Role of laser-induced melting and vaporization of metals during ICP-MS and LIBS analysis, investigated with computer simulations and experiments†

Davide Bleiner, Zhaoyang Chen, David Autrique and Annemie Bogaerts*

Received 23rd February 2006, Accepted 4th May 2006
First published as an Advance Article on the web 1st June 2006
DOI: 10.1039/b602800d

The role of surface melting and vaporization during laser ablation of several metals is investigated, presenting results from a numerical model and experimental determinations. The model takes into account the laser–solid interaction, melt-pool development and evaporation of the target material, followed by vaporization and plume expansion in 1 atm He background gas, plasma formation, and laser–plasma interaction. Surface melting and vaporization are shown to be responsible for the formation of a non-stoichiometric particle fraction. A comparison is made between several metals (Cu, Zn, Al, Fe, Mn and Mo) to evaluate whether they are potentially prone to fractionate in a laser-induced aerosol. It is found that the material properties, such as target surface reflectivity, optical absorption coefficient, thermal diffusivity, and melting/boiling temperature, have a pronounced influence on the target surface temperature and the amount of laser-induced vaporization. Consequently, the plume expansion, plasma formation and plasma shielding will also be different for different target metals. Our model predicts that the Al vapor yield is much lower than for the other metals, indicating that the ablation of Al should be mostly attributed to melt mobilization. The actual crater volume produced during laser ablation experiments using some target metals was directly measured, as a means to assess the role of surface vaporization on the overall mass removal extent. This showed a dependency on material and irradiance, so that for certain operating conditions surface vaporization cannot be neglected, potentially leading to fractionation. At low irradiance the micro-sampling process becomes less reproducible, both from the physical and chemical perspective. At high irradiance, phase explosion and droplet expulsion greatly enhance the ablation rate, leading to more regular sampling conditions.

1. Introduction

Laser ablation (LA) has become a mature technique for the elemental analysis of solid materials, either coupled to on-site optical emission spectroscopy using laser-induced breakdown spectrometry (LIBS) or as a material sampling method for inductively coupled plasma spectrometry (LA-ICP-MS or LA-ICP-OES).[1–6] Despite the widespread use in many analytical applications, the physical processes of laser ablation and laser-induced plasma formation are not yet fully understood.

Recently, we have developed a modeling network that describes laser–solid interaction, resulting in heating, melting and evaporation of the target, as well as evaporated plume expansion in 1 atm background gas, plasma formation, and plasma shielding of the laser radiation.[7,8] Particle formation, due to either condensation in the expanding plume, liquid splashing, or explosive boiling is not yet included in the model, but are the object of current work. The model was initially developed for the ablation of Cu, with expansion in a vacuum,[9,10] and later extended to expansion in 1 atm He gas.[7,8] A wide range of laser conditions (irradiance, pulse duration and wavelength)[11] were investigated, as well as the expansion in other rare gases or in N_2,[12] and a variety of different background gas pressures, ranging from vacuum to above 1 atm.[13] So far, ablation characteristics have been simulated for Cu as the target material. However, due to different optical and thermal properties (*e.g.*, target surface reflectivity, optical absorption coefficient, thermal conductivity, melting and boiling point), these results cannot be generalized to other metals.

Horn *et al.*[14] measured the ablation rate for different samples (*i.e.*, Al, Cu, Si, Mo, Ti, CaF_2 and glass), with an excimer laser at 193 nm and an Nd:YAG laser at 266 nm, at a laser fluence between 3.5 and 35 J cm^{-2} (or laser irradiance approximately between 1 and 10 GW cm^{-2}). They observed clear differences in the ablation rates for different materials, but could not identify a direct correlation between ablation rate and melting or boiling point, thermal conductivity or reflectivity.

In contrast, Sallé *et al.*[15] suggested a definite effect of the material melting point. They investigated different metals (Mo, Fe, Mn, Cu, Al, Zn, Pb and Sn) in air at 1 atm, using an excimer laser KrF* at 248 nm and a solid-state laser Nd:YAG at 266 nm, with a laser irradiance between 0.5 and 50 GW cm^{-2}, and found that a lower melt temperature yielded a larger crater depth and diameter.

University of Antwerp, Department of Chemistry, Universiteitsplein 1, BE-2610 Antwerp, Belgium. E-mail: annemie.bogaerts@ua.ac.be
† Presented at the 2006 Winter Conference on Plasma Spectrochemistry, Tucson, AZ, USA, January 8–14, 2006.

Furthermore, Cabalín and Laserna[16] compared laser-induced breakdown thresholds for several pure metals, selected according to their different thermal and physical properties (particularly melting and boiling point and thermal conductivity), with an Nd:YAG laser at 1064 nm, 532 nm and 266 nm, at a laser fluence in the range of 1–40 J cm^{-2}. They found a reasonable correlation between fluence thresholds for plasma formation and thermal properties such as melting and boiling points, indicating that with ns-pulse lasers, and also at UV laser wavelengths, the photothermal mechanism of LA cannot be neglected. These findings were also confirmed in a recent paper from this group,[17] using one Nd:YAG laser at 532 nm and laser irradiance values between 14 and 1000 MW cm^{-2}, where a clear correlation was obtained between threshold fluence for plasma formation and melting temperature of various metals. No correlation was found with the first ionization potential or the work function of the different metals.

Finally, in a comparison between Cu and Al targets, performed in ref. 18 with an Nd:YAG laser at 1064 nm and a laser irradiance of 1 GW cm^{-2}, it was found that the plume temperature is much higher for Cu than for Al. This was attributed to the higher melting point of Cu yielding less material ablation but a higher plume temperature, because the laser energy was distributed to a lower number of particles.

Hence, it is clear that there is a need for a systematic study of the relation between the laser ablation behavior of different metals and their thermo-optical properties. Since our model focuses on the *thermal mechanisms* of laser ablation, it is particularly suitable to perform such a systematic study. The present paper makes a comparison between several different metals, *i.e.*, Al, Mn, Fe, Cu, Zn, Mo and Pb. Moreover, crater profiles were also measured experimentally for some targets. Based on the comparison between theoretical results and experimental observations, more insights can be obtained about the effect of thermal and optical mechanisms in the laser ablation process of metals.

2. Description of the model

The model for laser ablation of metallic targets and plume expansion in 1 atm background gas was explained extensively in ref. 8, and hence will not be repeated here in detail. Briefly, it describes the following steps of laser ablation:

(1) laser–solid interaction, melting and evaporation of the metal target, which is described with a 1-D heat conduction equation;

(2) vapor plume expansion in 1 atm background gas, calculated with fluid dynamics equations, such as continuity equations of vapor mass density, total mass density (vapor + background gas), momentum (Navier–Stokes equation) and energy;

(3) plasma formation in the expanding vapor plume, where (because of the collisional regime) the local thermal equilibrium (LTE) approximation was made, which means that the ionization degree can be calculated with the Saha equation;

(4) laser–plasma interaction due to inverse Bremsstrahlung and photo-ionization, resulting in shielding of the incoming laser radiation.

It should be noted that other processes might also happen in practice, depending on the conditions, such as nanoparticle formation in the expanding vapor plume, splashing of the molten target, and explosive boiling of the target. These processes are not yet included in the model.

The model is applied to six different metals, *i.e.*, Cu, Zn, Al, Fe, Mo and Mn. Their characteristic thermal and optical properties, as well as their ionization potentials as needed in the model equations, are summarized in Table 1. These data were taken from ref. 19. Note that the values for the heat capacity, thermal conductivity, thermal diffusivity and mass density are different for the solid and molten phases; the latter are presented within parentheses. The values for the target surface reflectivity, R, are calculated from:

$$R = \left|\frac{n-1}{n+1}\right|^2 \qquad (1)$$

where n is the refractive index, which is dependent on the laser wavelength and the kind of material, and is taken from ref. 19.

Calculations are performed for an Nd:YAG laser at 266 nm, with 5 ns pulse duration (FWHM) and Gaussian-shaped time-profile, and a laser irradiance of 1 GW cm^{-2}, unless mentioned otherwise. The background gas is assumed to be He at 1 atm.

Table 1 Thermal and optical properties of the different metal targets investigated in this work. The data are taken from ref. 19. The heat capacity, thermal conductivity, thermal diffusivity and mass density of the metals are different in the solid and molten states. The corresponding values in the molten state are given in parentheses

Metal	Al	Mn	Fe	Cu	Zn	Mo	Pb
Heat capacity, C_p/J kg^{-1} K^{-1}	897 (920)	479 (590)	449 (507)	420 (494)	430 (480)	251 (275)	130 (142)
Thermal conductivity, λ/W K^{-1} m^{-1}	237 (110)	7.82 (4.0)	80.2 (34.5)	380 (170)	116 (60)	138 (70)	35 (31)
Thermal diffusivity, D_h/ $\times 10^{-5}$ m^2 s^{-1}	9.8 (5.0)	0.22 (0.1)	2.3 (1.0)	10.1 (4.3)	3.8 (2.0)	5.4 (2.7)	2.4 (2.1)
Optical absorption coeff., $\alpha/10^7$ m^{-1}	15.1	9.2	7.5	7.4	7.7	18.1	14.9
Mass density, ρ/kg m^{-3}	2700 (2375)	7440 (5950)	7874 (6980)	8960 (8000)	7130 (6210)	10 200 (9330)	11 340 (10 600)
Surface reflectivity at 266 nm, R_f	0.92	0.38	0.47	0.34	0.77	0.66	0.70
Melting point, T_m/K	933	1519	1808	1358	693	2896	601
Boiling point, T_b/K	2792	2335	3023	2836	1179	4912	2022
Heat of fusion, ΔH_{fus}/kJ mol^{-1}	11	15	14	13	7	37	4
Heat of evaporation, ΔH_{ev}/kJ mol^{-1}	290	220	350	300	1.10	590	190
First ionization potential, IP_1/eV	5.99	7.43	7.90	7.73	9.39	7.09	7.41
Second ionization potential, IP_2/eV	18.83	15.64	16.18	20.29	17.96	16.16	15.03

3. Experimental

A laser microsampler Nd:YAG (Quanta-Ray DCR-11, Spectra-Physics) was modified in-house to obtain UV radiation with the fourth harmonic. Frequency-quadrupled wavelength (266 nm, Q-switched with a 6 ns pulse length) light was focused using a 40 mm focal distance objective lens. A nominal spot size of 100 μm was used at two energy attenuation settings, which resulted in a fluence of 1.1 GW cm^{-2} and 6.2 GW cm^{-2}. In the following, we have referred to the two irradiance settings as 'low' and 'high' irradiance, respectively. In both cases 200 pulses were delivered onto the static target, at a repetition rate of 10 Hz. Targets of Al, Cu, Fe, and Zn were ablated. Three different craters per sample at each irradiance setting were ablated.

A Tencor P-10 profilometer was used to obtain traces of the surface profile, and thus the crater morphology. Three traces ($n = 3$) per crater were acquired with a stylus load of 5.0 mg and a moving speed of 20 μm s^{-1} over a distance of 500 μm. The traces were integrated to obtain the ablated volume, the depth, and absolute removed mass.

4. Results and discussion

4.1. Calculated surface temperature, and relation to material properties and phase change

Fig. 1 shows the calculated temperature distributions inside the target materials, as a function of time. In all cases, the temperature reaches a maximum at the surface when the laser pulse reaches its peak value, *i.e.*, at about 8 ns. However, there are significant differences in the calculated values of the maximum temperature, ranging from *ca.* 3000 K in the case of Zn and Al, above about 7000 K for Fe, Cu, and Mn, and above 10 000 K in the case of Mo (see scales for exact values). This pronounced difference in target surface temperature, as

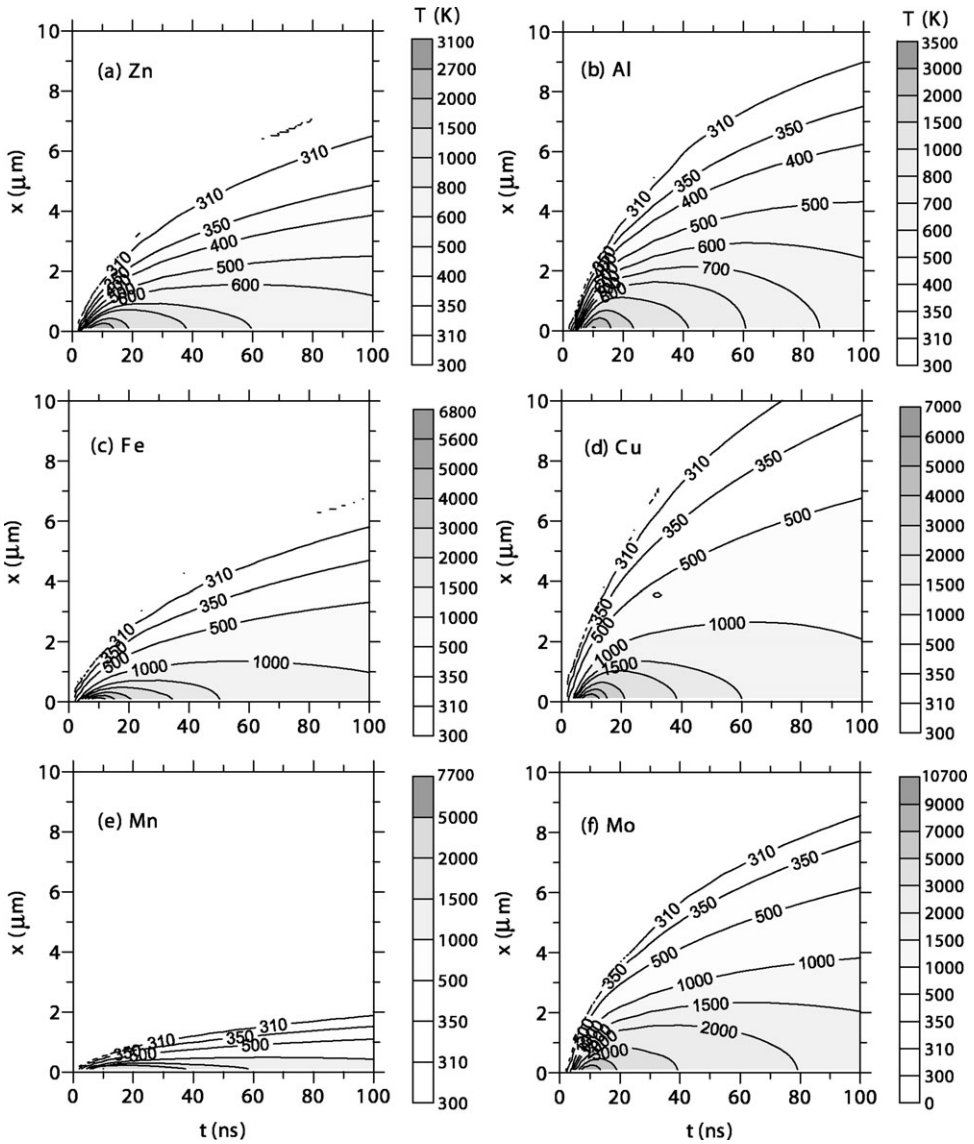

Fig. 1 Calculated temperature distributions inside the target, as a function of time, for the six different metal targets investigated, for an Nd:YAG laser at 266 nm, with 5 ns pulse duration (FWHM) and a laser irradiance of 1 GW cm^{-2}.

well as in the temperature distribution inside the target, is mainly attributed to the different target surface optical absorption coefficients, reflectivities, and thermal diffusivity, given in Table 1.

The *optical absorption coefficients* of Al and Mo are higher than that of the other metals, which means that laser energy is more strongly "coupled" per unit length in the material, and hence can be used for heating at or beneath the surface. This partially explains the high surface temperature in the case of Mo, and the somewhat higher surface temperature of Al, compared to Zn, in spite of the high surface reflectivity of Al.

Al and Zn have high *surface reflectivities* of 0.92 and 0.77,[19] respectively, which means that only 8% and 23% of the laser irradiance is transmitted to the target, and can be used for heating of the material. This percentage applies to the laser irradiance that reaches the target past the laser-induced plume, which in turn partially shields the beam in an irradiance-dependent way.[11] This explains why Al and Zn are characterized by the lowest target surface temperature, as predicted by our simulations.

Tabulated values of reflectivity are typically given at room temperature, with the indication that they are a function of temperature. However, all reported experimental fits of the reflectivity–temperature dependence are obtained under equilibrium conditions, *i.e.*, the temperature of the test material is modified and after a characteristic equilibration time the reflectivity, or another related parameter,[20] is measured. This approach does not apply to laser irradiation of materials, especially for high power and short pulse systems. In fact, under fast heating regimes (above 10^8 K s^{-1}),[21] as is typical for ns-pulse LA, the material passes *quickly* from a standard condition to a critical point condition, in a non-continuum transition (first-order phase change).

It has been reported that at 80–90% of the critical point the irradiated material's physical properties begin to be (rapidly) modified in an analytical way (*i.e.*, smooth continuum changes).[21] This second order phase transition does not involve any latent heat like the first order counterpart, and it is realized without a "mixed-phase regime" (as in normal melting and boiling). For instance, McMordie *et al.*[22] have measured the reflectivity of Al as a function of laser irradiance, using a CO_2 laser of 2–3 μs pulse width, showing a plateau up to 10^3 W cm^{-2} and a sudden (factor of 4) reduction of reflectivity at higher irradiance (inverted sigmoid profile). Thus, for fast heating rates and sub-critical conditions, the reflectivity value is that of the initial state, as long as *activated* melting and vaporization are involved.

However, close to the critical point, phase explosion[23] is believed to be the dominating process.[21] This ablation mechanism has not yet been included in our model, for both theoretical and practical reasons. Theoretical reasons refer to the characteristics of this process, which is a second-order phase change process. This means that the mathematical treatment is very different from the one implemented so far to describe melting and vaporization, where the numerical solution had to face with a Riemann singularity.[8] Phase explosion induces the formation of a different phase from the ones triggered during melting and vaporization, with its own size distribution, composition, and ejection dynamics.

Moreover, in practical terms, there is a deep interest in melting and vaporization specifically, as these are considered to be potentially responsible for the non-stoichiometric sampling ("fractionation effects") of aerosols used for elemental and trace analysis.[24,25] Of course, we are allowed to neglect the explosive boiling as long as we are not concerned about absolute mass balances, in which case phase explosion should be considered (absolute quantification), as indeed will be done in future work. Here it should be remarked that only computational studies are suitable for investigating the role of melting and vaporization individually and independently from other simultaneously occurring ablation mechanisms.

The third parameter, which mainly determines the temperature distribution inside the target, is the *thermal diffusivity*, which is the ratio of thermal conductivity to heat capacity and density, *i.e.*, $D_h = \kappa/(c_p\rho)$. Substances with high thermal diffusivity rapidly adjust their temperature to that of their surroundings, because they delocalize heat quickly to their bulk. This parameter is highest for Cu and Al (Table 1), which explains also why the heat extends further inside the target materials (Fig. 1b,d). On the other hand, Mn has a very low thermal diffusivity, which explains why a significant temperature rise was only observed in the first couple of micrometres beneath the surface (Fig. 1e).

All these physical parameters interplay and contribute to the overall outcome in terms of material response, surface recession rate, and abundance of melting *versus* vaporization during the laser-induced energy deposition. The energy directed to the target, past the attenuation across the plume, is delocalized in a two-fold way: *back* into the ambient by means of surface reflection or *inside* the bulk by means of heat diffusion. The input energy, E_0, delivered to the target surface is transmitted, as $E_t = E_0\,(1 - R)$, into the material for the heating. The heating regime was characterized using the Tokarev–Kaplan product, $K = \alpha^2 D_h \tau$,[26,27] of the optical absorption coefficient (α), thermal diffusivity (D_h) and pulse duration (τ). For small values of K, especially less than 1, the heating is volumetric, otherwise it is a surface process.

To obtain a complete picture of the effect of the various discussed thermo-optical parameters, we introduce the *phase change capability* index. The material-dependent phase change capability was computed as the ratio between the radiation energy transmitted into the material and the energy required for heating and for melting or vaporization the material, as follows:

$$X = \frac{(1 - R)}{\sum_i (c_p^i \Delta T^i + L^i)} \qquad (2)$$

The summation of the energy demand at the denominator of eqn (2) was extended to all "i" steps of phase transition, *i.e.*, one step for melting (solid–liquid) or sublimation (solid–vapor), and two steps for evaporation (solid–liquid–vapor). The $c\Delta T$ term in the denominator of eqn (2) accounts for material heating, and the second term L for the phase change enthalpy (latent heat). The radiation energy is normalized ($E_0 = 1$) and taken as constant for all metals, *i.e.*, we neglected here the material-dependent plume shielding, in order to evaluate specifically the effect of the thermo-physical

properties of each target. However, in the fluid dynamical simulation code, whose results are shown below, plume shielding was considered and coupled into the calculations of phase change.

Eqn (2) tells us that a metal with high reflectivity and low melting/boiling point and enthalpy should, in principle, behave similarly to another that has lower reflectivity but higher melting/boiling point. Hence, the balance between coupled energy and energy demand per unit volume determines the material response. Thus, we divided eqn (2), which is only an energy ratio, by the Tokarev–Kaplan product shown above, to account for spatial delocalization of the energy.

Fig. 2 shows the relative probability for both melting and for vaporization (either sublimation or evaporation), for the set of target metals investigated. In addition to the six metals investigated in the simulations, Fig. 2 also shows results for Pb, because this element exhibits some peculiar behavior, known from experiments.[24] The thermal and optical data for Pb are therefore also included in Table 1. It is notable that the melt formation is always more probable than the vaporization capability, due to lower energy demand (note the *y*-axis break). The melt formation tendency is exacerbated for Al and Pb, according to their thermo-optical properties.

These values are in agreement with experimental values, although exact experimental proportions are irradiance-dependent. Fishburn *et al.*[28] showed that at low fluences material removal occurs by both vaporization and melt displacement in Al, whereas at high fluences (>7 J cm^{-2}) material removal is predominantly by explosive ejection of liquid droplets from the melt pool, with as low as 10% removed as vapor. Recalling that material removal by means of melt expulsion is at least a factor of 4 more efficient than surface vaporization, as discussed in ref. 29, Fig. 2 can be read as an explanation for the experimentally observed element-dependent crater morphologies, as will be shown below.

In Fig. 2 it is also notable that for Pb the probability of evaporation and sublimation is almost identical, which greatly enhances the direct transfer of Pb from solid into the vapor phase. In the case of the other metals, this passage is conditioned by the presence of a melt phase (evaporation). However, due to the rapid heat transfer under ns-pulse LA, the material, once molten, might not have the time to further change extensively into vapor. The fact that Al, and most notably Pb, deviate from the trend of the majority of metals in terms of their melting/vaporization behavior, provides an explanation for fractionation effects in the laser-generated particles from Al- or Pb-bearing samples, as reported in the literature.[30]

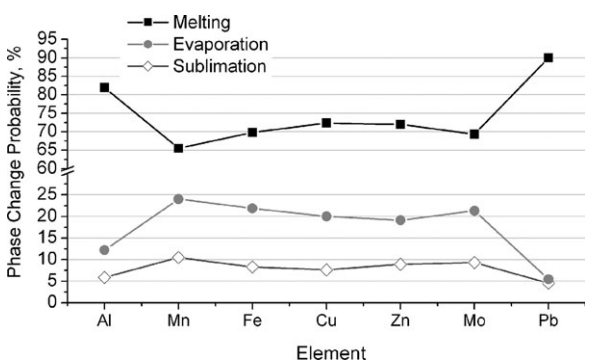

Fig. 2 Phase change probability calculated with eqn (2) corrected with the Tokarev–Kaplan product (see text for discussion). Al and Pb show the highest tendency to produce melt. Additionally, Pb can sublimate (unlike the other metals) instead of requiring a two-step transition to vaporize (melting and then evaporation).

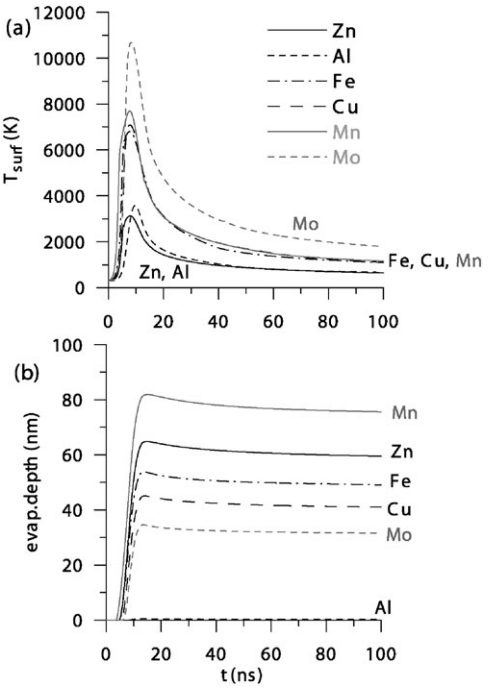

Fig. 3 Calculated surface temperature (a) and evaporation depth (b), as a function of time, for the six different metal targets investigated, at the same laser conditions as in Fig. 1.

4.2 Calculated melt and evaporation depths

Fig. 3(a) shows the simulated temperature rise in the various metals and Fig. 3(b) gives the corresponding calculated evaporation depth induced. Note that the evaporation depth increases drastically within a short time (about 10 ns, *i.e.*, during the laser pulse), and then the evaporation saturates and the depth reduces slightly, because the evaporation process has ceased (the laser pulse is over) and re-condensation at the target starts to occur. Back-flux to the surface is given by the Hertz–Knudsen equation.[8] Although Mo reaches the highest surface temperature, the evaporation depth is calculated to be only 32 nm, which is lower than for most other metals, due to its low thermal diffusivity and high boiling temperature. Cu and Fe have similar surface and boiling temperatures, hence their evaporation depths are also comparable (in the order of 45–50 nm). For Zn, the calculated evaporation depth is relatively high (around 60 nm), in spite of its low surface temperature, but this is because of its low boiling temperature. Mn appears to have the highest evaporation depth, of about 80 nm (attributed to its high surface temperature and relatively low boiling temperature), whereas for Al the model predicts a very low evaporation depth, of only 0.3 nm, due to its rather

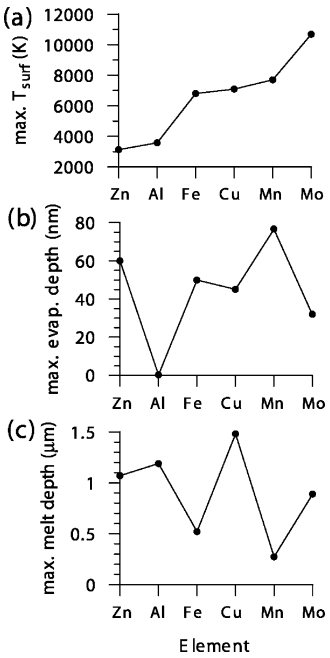

Fig. 4 Calculated maximum surface temperature (a), evaporation depth (b) and melt depth (c), for the six different metal targets investigated, under the same laser conditions as in Fig. 1.

low attained surface temperature (3580 K), in comparison with its boiling temperature (2790 K). In the light of the discussion made above on the interplay of physical properties, the low evaporation depth computed is not in contradiction with experimental observations,[14,15] where Al showed a greater crater depth than most other metals, as shown below.

The calculated maximum surface temperature and evaporation depth are plotted in Fig. 4a,b, together with the predicted melt depth, Fig. 4c, for the different metals. The melt depth seems to range from 300 nm in the case of Mn, to almost 1.5 μm for Cu. This trend is strongly correlated with the thermal conductivity of the different metals. Indeed, Mn has a very low thermal conductivity (Table 1), so that the temperature rise is limited to a narrow region just underneath the surface (Fig. 1e); hence the melt is also limited to a narrow region below the surface. Cu, on the other hand, has a very high thermal conductivity (Table 1); hence the heat is spread across a wider region inside the target (Fig. 1d), resulting in a larger melt depth, as is indeed clear from Fig. 4c. Naturally, the surface temperature and melting point of the different materials also determines the melt depth. The low melting point of Al and Zn, for instance, explains why these metals have a relatively large melt depth, in spite of their rather low surface temperature. This result is in agreement with the data presented in the literature.[14,15] This suggests that, at least for certain metals such as Al, laser-induced evaporation is not the main mechanism resulting in material ablation, but that melt ejection might also play an important role. Indeed, in refs. 15–17 a correlation was reported between crater depth (or fluence threshold for plasma formation) on one hand, and melting point of different metals on the other hand.

4.3. Calculated laser-induced plume characteristics

Fig. 5 illustrates the vapor plume expansion in the case of laser ablation of a Zn target, at 8 ns (a), 50 ns (b) and 100 ns (c) of the laser ablation process. The upper row of plots represents time slices of the Zn vapor and He background gas number density, as well as the corresponding neutral fractions. The plots in the central row show the charged particle number density (vapor and background gas), as well as the electron number density. Note that the total electron density consists of contributions from the vapor, *i.e.*, the density of Zn^+ plus twice the density of Zn^{2+}, and the background gas, which is equal to the He^+ density. As shown below, the latter is generally of minor importance. In the bottom row, the temperature distribution inside the plume is shown.

At 8 ns (Fig. 5a), the Zn vapor has a very high density, much higher than the background gas density, because laser-induced evaporation is at its maximum. The vapor density has its maximum at the target, because of the target evaporation process. The background gas is pushed away from the target, resulting in a compression front with a density in the order of 8×10^{25} m^{-3}, which is about a factor of three higher than the undisturbed background gas density in the ablation cell, about 2.5×10^{25} m^{-3} (value calculated at 1 atm and room temperature).

Because of the high temperature of approximately 50 000 K at its maximum, the vapor plume turns into a plasma, and the Zn vapor is almost fully ionized. Indeed, the neutral (Zn^0) density is very low compared to the Zn^+ and Zn^{2+} number densities, which are found to be more or less comparable in magnitude, with the Zn^{2+} density being higher than the Zn^+ density. Therefore, the electron number density reaches values in the order of almost 5×10^{26} m^{-3}, near the target, but it drops significantly as a function of distance from the target, in the same way as the Zn vapor. Indeed, the He background gas is more or less in a neutral state, and hence does not contribute to charged particle creation, and hence to the electron density.

At 50 ns, and later at 100 ns (Fig. 5b,c) the situation has changed, because target evaporation has ceased. The Zn vapor density does not reach its maximum near the target, but is spread along the plume, and is much lower than both the density at 8 ns and the He background gas density (in the order of 5×10^{24} to 10^{25} m^{-3}). The compression front of the He background gas density is very pronounced.

On the other hand, the plume temperature is slowly decreasing as a function of time, with typical values in the order of 20 000–30 000 K, at 50–100 ns. At these temperatures, the Zn vapor is still almost completely ionized, but the Zn^+ fraction is now higher than the Zn^{2+} fraction (except near the maximum of the plume temperature). Also the He background gas now has a small contribution to the charged particle densities, which is mainly attributed to the much higher He gas density, because the ionization degree of the He gas is typically much lower than that of the metal vapor (as will also be illustrated below). From Fig. 5, it is clear that the plume temperature is still rather high at 100 ns, resulting in a large fraction of charged particles in the plume.

In Fig. 6, the plume characteristics for the six different metal targets investigated are compared. Note that the plume in our

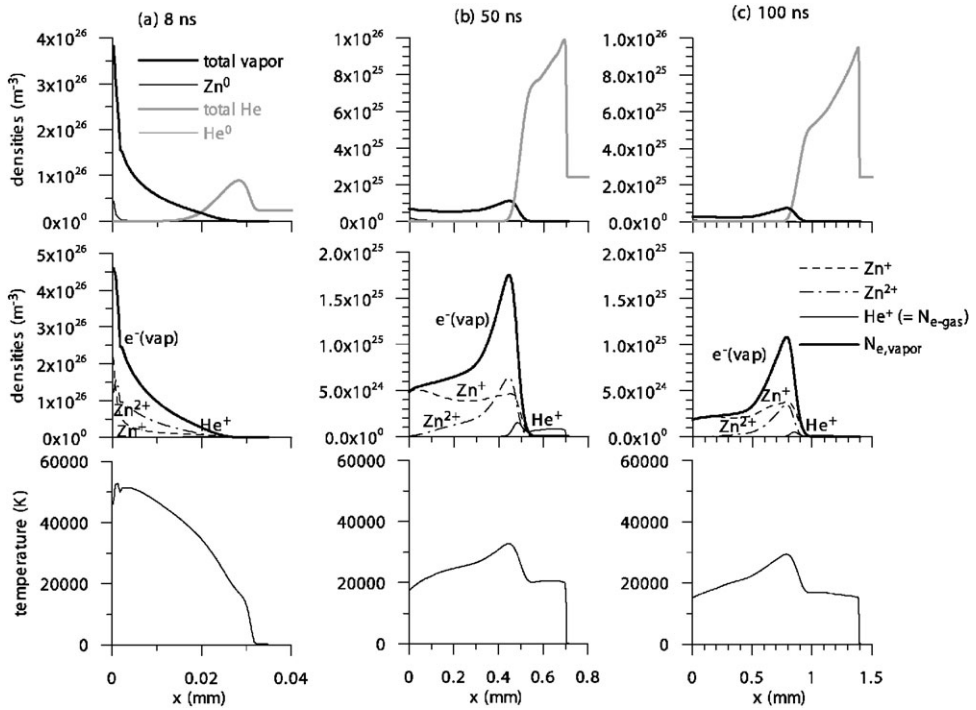

Fig. 5 Calculated plume characteristics for Zn vapor plume expansion in 1 atm He background gas, at 8 ns (a), 50 ns (b) and 100 ns (c), under the same laser conditions as in Fig. 1. The upper set of figures represent the density profiles of total Zn vapor and He background gas, as well as the densities of Zn and He atoms. The middle set of figures illustrate the density profiles of Zn^+, Zn^{2+} and He^+ ions, as well as the electron number density profile. The lower set of figures show the temperature distribution inside the plume.

calculations consists only of evaporated material in atomic form, and not clusters or solid particulates. In Fig. 4 the data for the different metals were plotted as a function of rising target surface temperature, but it was observed that a higher surface temperature did not always yield a higher evaporation depth. In Fig. 6, the data are plotted for the six metals in order of rising evaporation depth, because the amount of evaporation naturally determines the plume characteristics. Indeed, as is clear from Fig. 6a, the metal vapor number density increases drastically, going from Al to Mn, in close correlation with the evaporation depth (Fig. 4b). The same applies to most of the other plume characteristics, *i.e.*, maximum background gas density (Fig. 6b), the plume velocity (Fig. 6c), plume length (Fig. 6d), shock front position (Fig. 6e), maximum plume temperature (Fig. 6f), ionization degree of the metal vapor (Fig. 6g) and maximum electron density (Fig. 6i). Note that the plume length symbolizes the position where the vapor density has dropped to negligible values, whereas the shock front position denotes the end of the background-gas compression front. This is typically a few tens of mm further away from the target, as is clear from Fig. 5.

Al shows very different properties to the other metals, which is attributed to the very low amount of evaporation of Al at 1 GW cm^{-2}, as calculated with the model. Indeed, our model calculations predict that at 1 GW cm^{-2}, virtually no vapor plume is formed in the case of Al. We also performed calculations for a laser irradiance of 2 GW cm^{-2}, in the case of Al, and the results are indicated with a star (☆) in Fig. 6. Even at 2 GW cm^{-2}, the Al vapor density, plume velocity, plume length, plume temperature, ionization degree and electron density are still calculated to be lower than the corresponding values for the other metals at a laser irradiance of 1 GW cm^{-2}. There are not many experimental data available in the literature about the plume characteristics for laser ablation of different metals. In ref. 18 a lower plume temperature was reported for Al than for Cu, which is, at least qualitatively, in agreement with our predictions.

A further consideration should be made when comparing Fig. 6g and Fig. 6h. It is clear that the ionization degree of the He background gas is considerably lower than the ionization degree of the metal vapor. Indeed, He has a much higher ionization potential (24.58 eV) than the metal atoms (in the range 7–9.4 eV, as shown in Table 1), and even the second ionization potential of the metals is lower than the first ionization potential of He. Whereas the He gas is almost completely in atomic form, the metal vapor is mainly singly ionized (M^+) and even doubly ionized (M^{2+}), except for the case of Al, which is still mainly in atomic form at the laser conditions under study, because of the low plume density and temperature.

4.4. Calculation of energy absorption in the laser-induced plasma

The trends observed in the plume/plasma characteristics can also be translated to the process of laser–plasma interaction. Indeed, it is obvious that higher number densities of electrons and metal vapor in the plume result in more electron–ion and electron–neutral inverse Bremsstrahlung (*e-i* IB and *e-n* IB), and consequently in more laser–plasma interaction. Fig. 7

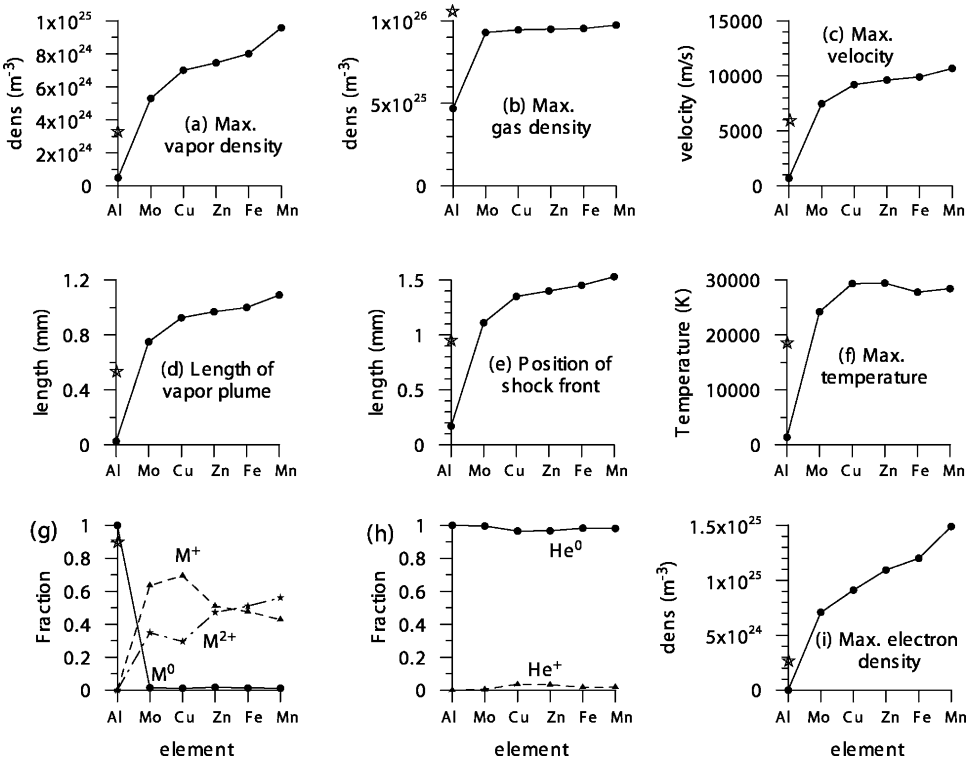

Fig. 6 Calculated maximum metal vapor density (a), maximum He background gas density (b), maximum plume velocity (c), vapor plume length (d), position of shock front (e), maximum plume temperature (f), fraction of M^0, M^+ and M^{2+} in the metal vapor (g), fraction of He^0 and He^+ (h) and maximum electron density (i), at 100 ns, for the six different metal targets investigated, at the same laser conditions as in Fig. 1. Because our model calculations predict that Al yielded almost no target evaporation, and hence plume formation, at a laser irradiance of 1 GW cm^{-2}, calculations for Al were also performed for a laser irradiance of 2 GW cm^{-2} and the results are illustrated with a star (☆) on the *y*-axes.

shows the laser irradiance time-profiles for the six different metals, as input values (solid lines), as well as the irradiance transmitted to the target, through the plasma (dashed lines). Note that a laser irradiance of 1 GW cm^{-2} is considered in all cases, except for the case of Al, where a value of 2 GW cm^{-2} is adopted, because at 1 GW cm^{-2} virtually no plume was formed, and hence the laser–plasma interaction was calculated to be zero. Even at 2 GW cm^{-2}, the laser–plasma interaction in the case of Al was very weak, yielding only 7% of laser absorption in the plasma. For the other metals, the laser–plasma interaction was found to be much more pronounced, even at a laser irradiance of 1 GW cm^{-2}, yielding higher plasma absorption values: 25% for Mo, 48% for Cu, 63% for Zn, 62% for Fe, and 78% for Mn, as shown in Fig. 8a.

Fig. 8b illustrates the relative contributions of *e-n* IB, *e-i* IB and photo-ionization (PI), for the different metals investigated in the computation. Apart from the case of Al, where the plasma laser absorption is found to be negligible due to a modest evaporation, *e-n* IB is found to be the dominant plasma absorption mechanism for all metals, whereas *e-i* IB and PI both contribute about 5%. This explains why the amount of plasma absorption correlates so well with the electron and metal vapor number densities. The fact that *e-n* IB is the most important laser absorption mechanism in the plasma was also found in our earlier modeling investigations for a wide range of laser irradiances and pulse durations,[11] and for different background gases.[12] Only at longer laser wavelengths (*e.g.*, 532 or 1064 nm), does *e-i* IB become an important absorption mechanism, especially at high irradiance values.[11]

4.5. Experimental validation of laser ablation characteristics

Fig. 9 shows crater profiles at the low and high irradiances (as defined in the Experimental section), with corresponding crater aspect ratios (AR), *i.e.* the depth-to-width ratio, as is common for characterizing the ablated crater morphology.[31,32] These experimentally determined profiles were used for (i) the validation of the theoretical results predicted by the numerical model, and (ii) to investigate potential causes of non-representative sampling, leading to non-accurate analytical determination (so-called "fractionation" effects[25]).

At low irradiance (Fig. 9, left-hand column) the crater morphology did not develop uniformly, and was more influenced by the beam energy profile. This suggests that although at low irradiance the depth resolution might be enhanced, the reproducibility of the micro-sampling becomes poor, especially for non-homogenized beams. Beam-profile homogenization is also important to have a reliable comparison with numerical results, especially at 1 GW cm^{-2}, which is the irradiance setting used during the numerical simulations.

At high irradiance (Fig. 9, right-hand column), a more regular pan-shaped morphology was produced, which seems to be the result of a more efficient and persistent material-

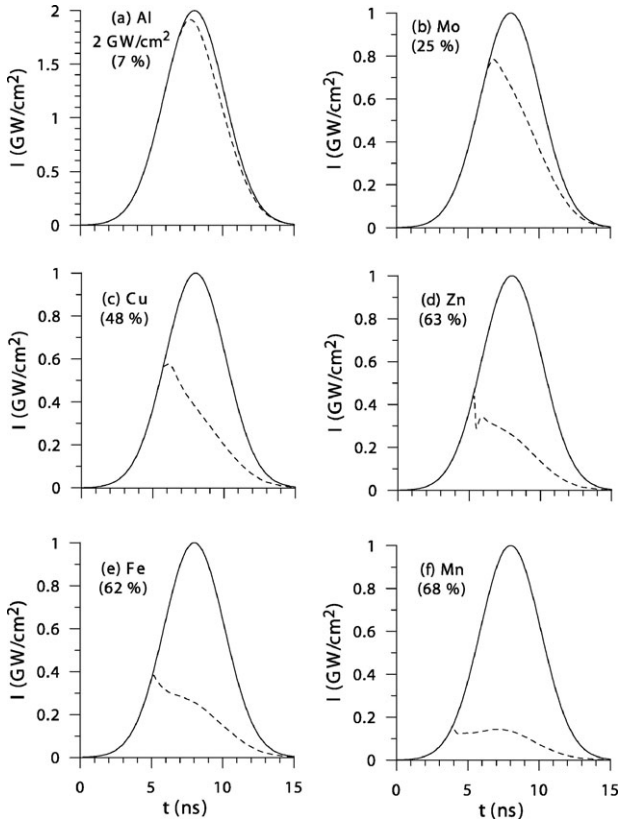

Fig. 7 Calculated laser irradiance time profiles, as emitted by the laser (solid lines) as well as the laser irradiance arriving at the target, after plasma shielding (dashed lines), for the six different metal targets investigated, under the same laser conditions as in Fig. 1. Note that for Al a laser irradiance of 2 GW cm^{-2} was assumed, because at 1 GW cm^{-2}, our model predicts no plasma shielding at all.

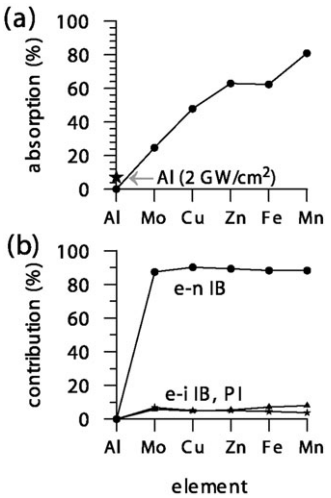

Fig. 8 Calculated relative amount of plasma absorption (a) and relative contributions of electron–neutral and electron–ion inverse Bremsstrahlung and photo-ionization (*e-n* IB, *e-i* IB, PI) (b), for the six different metal targets investigated, at the same laser conditions as in Fig. 1. For Al, the calculation results are also illustrated for a laser irradiance of 2 GW cm^{-2} (with a star (☆) at the *y*-axis).

removal mechanism. This must be connected with the formation and mobilization of a molten phase, as could also be inferred by the smooth appearance of the crater floor.

The surface recession rate is a sensitive function of target material thermo-physical properties. The craters on Al have the highest aspect ratio compared to the other metals, since for Al melt mobilization is the dominating mass removal mechanism even at very low fluence, as discussed above and reported in the literature.[28,33] For Al, vaporization was found to be approximately a factor of 2 less significant than most of the metals, which was also predicted by the numerical simulations. Indeed, at high irradiance the formation of 50 μm high walls around the Al pits is notable, due to extensive melt displacement at the crater periphery.

The craters in Cu were characterized by a wide surface extension, even at low irradiance. This effect can be attributed to the high thermal conductivity of this metal, which favors the formation of ablation pits larger than the nominal spot size.

Fe showed the most modest ablation efficiency, a result that can be explained by the tendency of Fe to ablate as a vaporized phase, which is also predicted by our computational study (a behavior similar to that of Mn).

In contrast, the crater on Zn shows soft-ablation characteristics, similar to the case of Al, with pronounced features, *i.e.*, direct impact of the donut beam profile in the inner shape, and large walls that can be attributed to melt displacement.

Fig. 10 shows the ablated volumes (a), the mass per pulse (b), the depth per pulse (c) and the crater width (d) obtained by integration of the crater profiles. The ablated volumes range from approximately 10^4 μm^3 up to slightly more than 10^6 μm^3, and they dramatically increase with laser irradiance. The highest ablated volume is noticed for Al, followed by Zn and Cu, whereas Fe has the lowest ablated volume. From the increase factors of ablated volume from low to high irradiance, shown in the histograms of Fig. 10a, it is clear that matrix-dependency is very important, a result that was also obtained in the numerical calculations (*cf.* Figs. 3 and 4).

Melting is strongly enhanced at higher laser irradiance. This trend is exacerbated in the case of Al, with an increase factor of 90, which is explained by the ''soft-ablation behavior'' for Al. Cu and Zn have comparable irradiance-dependency with increase factors of 20 and 18, respectively. Fe mass removal is very inefficient and its ''hard-ablation'' behavior is sensitive to the beam irradiance setting, as demonstrated by an increase by a factor of 60 from low to high power density. This indicates that the melt expulsion process of Fe is not so pronounced at low irradiance (higher threshold), as also demonstrated by the low crater volume at 1 GW cm^{-2} and the numerical simulations (see above). Thus, it can also be concluded that the relevance of melting and the droplet expulsion threshold is a function of target material stoichiometry.

The ablated mass given in Fig. 10b was calculated by multiplying the ablated volume by the mass density of the material, which is also given in the figure. The lower mass density of Al is responsible for the ''catch-up'' with the values of the other metals, so that the difference in terms of ablated mass is not as high as in the case of the ablated volume. Al showed absolute values of mass/pulse of 0.6 ng (low

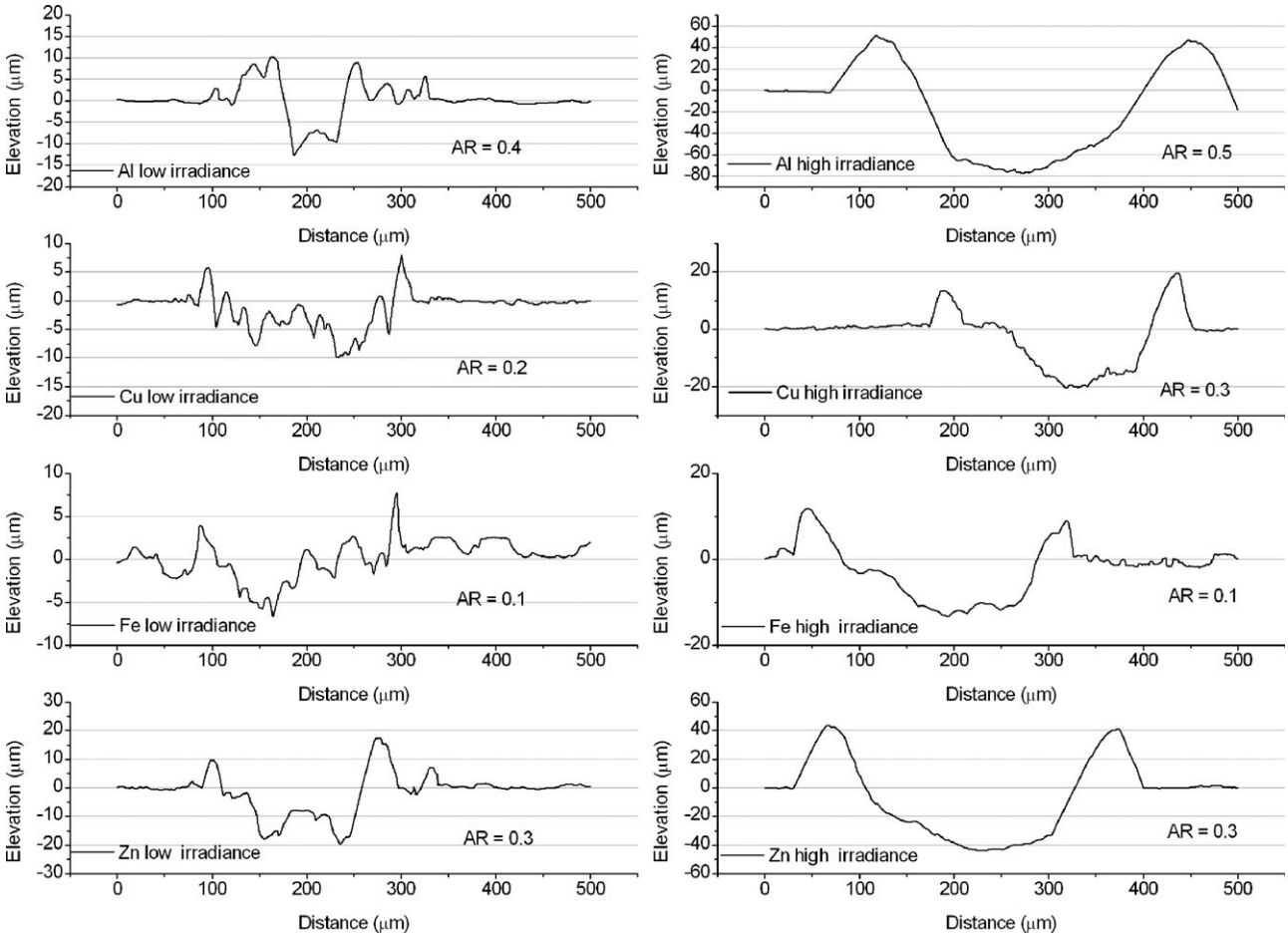

Fig. 9 Measured crater profiles at low irradiance (1.1 GW cm^{-2}) and high irradiance (6.3 GW cm^{-2}) for a selection of metals. Aspect ratio (AR) is the geometry parameter calculated as depth divided by width. The crater profiles are the average of three measurements, acquired with a moving speed of 20 μm s^{-1} over a distance of 500 μm. The craters were produced with 200 pulses of 266 nm delivered at a rate of 10 Hz. Note that the scale on the *y*-axis is different for the different plots.

irradiance) and 52 ng (high irradiance), whereas Cu showed values of 1.5 ng (low) and 31 ng (high), Zn of 3.7 (low) and 67 ng (high), and the depth/pulse in the case of Fe was 0.3 ng (low) and 18 ng (high). This would indicate that for less dense materials the damage zone is indeed larger, which can be theoretically explained following the Beer absorption model.

The ablated depth per pulse is plotted in Fig. 10c. Al showed absolute values of depth/pulse of 75 nm (low irradiance) and 406 nm (high irradiance), whereas Cu showed values of 54 nm (low) and 142 nm (high), Zn of 94 nm (low) and 237 nm (high), and the depth/pulse in the case of Fe was by far the lowest, 24 nm (low irradiance) and 83 nm (high irradiance). Hence, Al showed the strongest increase of depth per pulse with irradiance, namely a factor of 5.4. For the other materials increase factors were between 2.5 and 2.6 for Cu and Zn and 3.4 for Fe. However, notwithstanding similar increase factors, the absolute values for Cu and Zn were not similar, as indicated above.

A comparison with results from the numerical simulation shows that the calculated evaporated depths represent a lower bound for the experimental results, whereas the calculated melt pool depths are the upper bounds. The matching of the computational values with the experimental ones is closer to the lower or upper bounds, depending on whether the ablation of the metal is vapor-dominated (*e.g.* Fe) or melt-dominated (*e.g.* Al), respectively. Hence, from this comparison the predominant laser ''ablation'' mechanism can be deduced for the different metals.

The experimental values for Cu and Zn were approx. 15–30% higher than the computed evaporated depth at 1 GW cm^{-2}, which represent low-bound estimates. This comparison indicates that as little as 15–30% of the whole ablated mass was in the form of melt for these metals at 1 GW cm^{-2}.

Interestingly, for the case of Fe, the computational value of the evaporated depth is higher than the experimentally measured crater depth. This would suggest that for these conditions, the kinetics of phase change is playing a significant role. Under kinetic-controlled heat transfer and phase change(s), a delay in the onset of melting and vaporization is introduced with respect to the melting/boiling point. If the material is indeed superheated, the computational code, which assumes that phase changes occur exactly at the melting/boiling point, produces excess estimates. The importance of kinetics becomes evident for the case of Fe, because this metal provides the lowest measured depth/pulse values, so that in relative terms the approximation of neglecting heat transfer kinetics is larger.

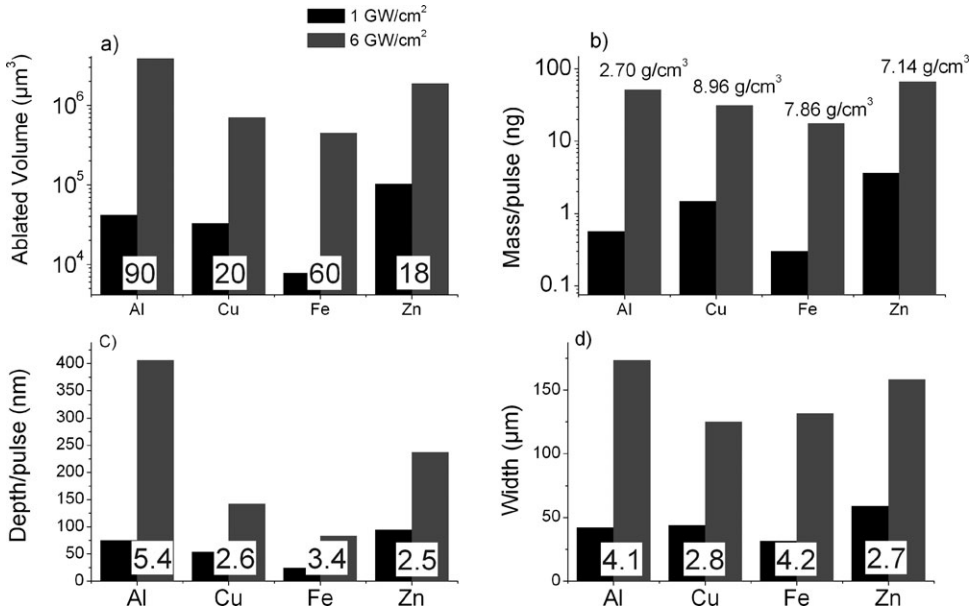

Fig. 10 The crater profiles acquired with surface profilometry were integrated to obtain the total ablated volume (a), the mass per pulse (b), the depth per pulse (c) and the geometric width (d). The crater width was obtained by dividing the cross-section crater areas shown in Fig. 9 by the crater depth. The values reported on the histograms are the enhancement factors from low to high irradiance.

The dependency of laser settings and ablation characteristics influences the quality of the micro-sampling, *i.e.*, stoichiometry, size distribution, depth resolution, *etc.* that can be attained in different metallic samples when LA-ICPMS or LIBS are used for depth profiling or elemental analysis. In depth profiling analysis, in the case of multi-layer samples, the user should be aware that the ablation speed is not uniform for different materials, which affects the depth scale calibration. Thus, mathematical strategies for data processing should be implemented.[34]

Finally, the crater width shown in Fig. 10d was obtained by dividing the cross-sectional area of each crater (from Fig. 9) by the depth. In this way the value obtained relates more directly to the morphology of the crater and can be associated to the entire ablated depth. This accounts more correctly for the 3D heat propagation across the target. In ref. 31 it was shown that the cross-sectional (depth-wise) profile of the craters can be fitted by a non-linear polynomial, which indicates that the relevance of mechanisms of material removal, *i.e.*, melt expulsion *versus* vaporization, changes as a function of depth. A reduction of melt expulsion with increasing depth has also been experimentally confirmed in studies of the particle size distribution during prolonged spot ablation.[35] Of course, the change of melt-to-vapor ratio with crater depth affects spatial resolution.

At low laser irradiance, the crater width is largest for Zn ($\sim$60 μm) and smallest for Fe ($\sim$30 μm). At the high laser irradiance, the crater width is about 120–130 μm for Cu and Fe, and it is about 160–170 μm for Zn and Al. Thus, both Al and Fe show an increase of crater width with irradiance of a factor of >4, in the investigated range, whereas Cu and Zn show an increase of a factor of <3. Therefore, for an identical numerical aperture and nominal spot size, the obtained lateral resolution is also a function of laser irradiance, material properties and ablated depth.

All these results permit us to conclude that the dependency among beam irradiance and ablated depth/width, or crater morphology, is not uniform for all metals. In some cases, *e.g.*, Fe, the more intense beam does not ablate more deeply (depth resolution is not proportionally affected), but rather the extra energy is redistributed across the surface to induce peripheral material removal. Thus, the ablated mass and the ablated depth did not scale similarly with beam irradiance for the different metallic targets.

5. Conclusions

We have investigated the effect of laser ablation on different metal targets, by means of a comprehensive modeling network that describes laser–solid interactions. The heating, melting and vaporization of the metal target, vapor plume expansion, plasma formation, and laser–plasma interaction were simulated. The model is applied to typical laser ablation conditions for elemental analysis, *i.e.*, an Nd:YAG laser at 266 nm, with 5 ns pulse width, and at a laser irradiance of 1 GW cm^{-2}, and an ablation cell filled with He gas at 1 atm. Several metals with different thermo-optical properties were compared during laser-assisted micro-sampling.

It was found that the material-dependent optical and thermal properties have a pronounced influence on the laser-induced target temperature for identical irradiation. For instance, Al showed the lowest surface temperature, in the order of *ca.* 3000 K, a factor of 3.5 less than Mo. Hence, we found that the ablation of Al is dominated by the formation of a melt phase, which enhances the development of a high aspect ratio crater. Instead, other metals, *e.g.*, Fe, showed a more significant role of the vapor phase in the surface recession mechanism. Thus, a rather significant metal-dependent laser micro-sampling efficiency is found, which is especially important for ICP-MS analysis.

In addition, for LIBS analysis we carefully investigated the vaporization of the targets, due to the correlation with the laser-induced plume characteristics, *e.g.*, the vapor and electron number density. In agreement with that discussed above, Al shows modest evaporation, and hence a very weak metal plume, without plasma formation, even at a laser irradiance of 2 GW cm^{-2}. The other metals exhibit a thick and opaque plume and almost fully ionized plasma even at 1 GW cm^{-2} irradiance. Consequently, our numerical computations clarified that the plumes of all metals can shield the incoming beam between 4 and 10 times more than the Al plume.

Experimentally determined crater profiles were also obtained and used for two main reasons:

(i) to validate the computational results predicted by the numerical model.

(ii) to investigate potential causes of non-representative sampling, leading to non-accurate analytical determination (so-called ''fractionation'' effects).

A comparison of experimental results with the numerical simulations shows that the calculated evaporated depths represent a lower bound for the experimental results, whereas the calculated melt depths are the upper bounds. For Al, the calculated vaporization depth was found not to match the experimental crater depth at all, which is consistent with a melt-dominated ablation mechanism. In contrast, for Fe vaporization was the dominating surface recession mechanism, which led to a greatly reduced ablation rate.

Moreover, not only the element-dependent dominating mechanism(s), but also the speed is very important. Melting and vaporization kinetics need to be taken carefully into account to explain the experimental ablation rates. For instance, the measured depths per pulse values for Fe (*i.e.*, a few tens of nm) mean that calculations considering complete phase change at the melting/boiling point sometimes might lead to excess estimates.

It should also be said that although at low irradiance the depth resolution might be enhanced, the reproducibility of the micro-sampling becomes poor, especially for non-homogenized laser beams. At high irradiance the formation and mobilization of a molten phase becomes more significant, which largely enhances the mass removal efficiency.

Acknowledgements

Z. Chen acknowledges financial support from a Bilateral Project between Flanders and China. D. Bleiner is financed by the Flemish Fund for Scientific Research (FWO). The authors thank A. Vertes for supplying the original code for laser ablation in vacuum, and R. Gijbels for interesting comments. Finally, EMPA Laboratories in Dübendorf (Switzerland) are acknowledged for the infrastructure used in the laser ablation experiments, carried out with the system managed by D. Bleiner at that time.

References

1 D. Günther, S. E. Jackson and H. P. Longerich, *Spectrochim. Acta, Part B*, 1999, **54**, 381–409.
2 R. E. Russo, X. Mao and S. S. Mao, *Anal. Chem.*, 2002, **74**, 70A–77A.
3 D. Günther, B. Hattendorf and C. Latkoczy, *Anal. Chem.*, 2003, **75**, 341A–347A.
4 L. J. Radziemski, *Spectrochim. Acta, Part B*, 2002, **57**, 1109–1113.
5 L. St.- Onge, V. Detalle and M. Sabsabi, *Spectrochim. Acta, Part B*, 2002, **57**, 121–135.
6 J. M. Vadillo and J. J. Laserna, *Spectrochim. Acta, Part B*, 2004, **59**, 147–161.
7 A. Bogaerts and Z. Chen, *J. Anal. At. Spectrom.*, 2004, **19**, 1169–1176.
8 Z. Chen and A. Bogaerts, *J. Appl. Phys.*, 2005, **97**, 063305.
9 L. Balazs, R. Gijbels and A. Vertes, *Anal. Chem.*, 1991, **63**, 314–320.
10 A. Bogaerts, Z. Chen, R. Gijbels and A. Vertes, *Spectrochim. Acta, Part B*, 2003, **58**, 1867–1893.
11 A. Bogaerts and Z. Chen, *Spectrochim. Acta, Part B*, 2005, **60**, 1280–1307.
12 A. Bogaerts, Z. Chen and D. Bleiner, *J. Anal. At. Spectrom.*, 2006, **21**, 384–395.
13 Z. Chen, D. Bleiner and A. Bogaerts, *J. Appl. Phys.*, 2006, **99**, 063304.
14 I. Horn, M. Guillong and D. Günther, *Appl. Surf. Sci.*, 2001, **182**, 91–102.
15 B. Sallé, C. Chaléard, V. Detalle, J. L. Lacour, P. Mauchien, C. Nouvellon and A. Semerok, *Appl. Surf. Sci.*, 1999, **138–139**, 302–305.
16 L. M. Cabalín and J. J. Laserna, *Spectrochim. Acta, Part B*, 1998, **53**, 723–730.
17 J. M. Vadillo, C. C. Garcia, J. F. Alcantara and J. J. Laserna, *Spectrochim. Acta, Part B*, 2005, **60**, 948–954.
18 A. Gomes, A. Aubreton, J. J. Gonzalez and S. Vacquié, *J. Phys. D: Appl. Phys.*, 2004, **37**, 689–696.
19 D. R. Lide, *CRC Handbook of Chemistry and Physics*, 83rd edn, CRC, Boca Raton, 2002.
20 G. Lohöfer, *Meas. Sci. Technol.*, 2005, **16**, 417–425.
21 M. M. Martynyuk, *Russ. J. Phys. Chem.*, 1983, **57**, 810–821.
22 J. A. McMordie and P. D. Roberts, *J. Phys. D: Appl. Phys.*, 1975, **8**, 768–781.
23 D. Bleiner and A. Bogaerts, *Spectrochim. Acta, B*, DOI: 10.1016/j.sab.2006.02.007.
24 P. M. Outridge, W. Doherty and D.C. Gregoire, *Spectrochim. Acta, Part B*, 1996, **51**, 1451–1462.
25 O. V. Borisov, X. Mao and R.E. Russo, *Spectrochim. Acta, Part B*, 2000, **55**, 1693–1704.
26 V. N. Tokarev and A. F. H. Kaplan, *J. Phys. D: Appl. Phys.*, 1999, **32**, 1526–1538.
27 D. Bleiner, *Spectrochim. Acta, Part B*, 2005, **60**, 49–64.
28 J. M. Fishburn, M. J. Withford, D. W. Coutts and J. A. Piper, *Appl. Surf. Sci.*, 2005, DOI: 10.1016/j.apsusc.2005.07.053.
29 K. T. Voisey, S. S. Kudesia, W. S. O. Rodden, D. P. Hand, J. D. C. Jones and T. W. Clyne, *Mater. Sci. Eng., A*, 2003, **356**, 414.
30 P. M. Outridge, W. Doherty and D. C. Gregoire, *Spectrochim. Acta, Part B*, 1996, **51**, 1451–1462.
31 O. V. Borisov, X. Mao and R. E. Russo, *Spectrochim. Acta, Part B*, 2000, **55**, 1693–1704.
32 A. Mank and P. Mason, *J. Anal. At. Spectrom.*, 1999, **14**, 1143–1153.
33 A. Lenk, B. Schultrich and T. Witke, *Appl. Surf. Sci.*, 1996, **106**, 473–477.
34 D. Bleiner, F. Belloni, D. Doria, A. Lorusso and V. Nassisi, *J. Anal. At. Spectrom.*, 2005, **20**, 1337–1343.
35 M. Guillong and D. Günther, *J. Anal. At. Spectrom.*, 2002, **8**, 831–837.